Renewable Energy 100 (2017) 129–140

Contents lists available at ScienceDirect

Renewable Energy

journal homepage: www.elsevier.com/locate/renene

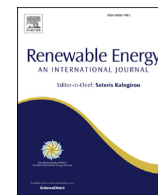

Multiscale modeling and run-to-run control of PECVD of thin film solar cells

Marquis Crose [a], Joseph Sang-Il Kwon [c], Anh Tran [a], Panagiotis D. Christofides [b, a, *]

[a] Department of Chemical and Biomolecular Engineering, University of California, Los Angeles, CA 90095, USA
[b] Department of Electrical Engineering, University of California, Los Angeles, CA 90095, USA
[c] Artie McFerrin Department of Chemical Engineering, Texas A&M University, College Station, TX 77843, USA

A R T I C L E I N F O

Article history:
Received 26 April 2016
Received in revised form
29 June 2016
Accepted 30 June 2016
Available online 12 July 2016

Keywords:
Process modeling
Plasma-enhanced chemical vapor deposition
Thin film solar cells
Multiscale modeling
Parallel computing
Run-to-run control

A B S T R A C T

In this work, we focus on the development of a multiscale modeling and run-to-run control framework with the purpose of improving thin film product quality in a batch-to-batch plasma-enhanced chemical vapor deposition (PECVD) manufacturing process. Specifically, at the macroscopic scale, gas-phase reaction and transport phenomena yield deposition rate profiles across the wafer surface which are then provided to the microscopic domain simulator in which the complex microscopic surface interactions that lead to film growth are described using a hybrid kinetic Monte Carlo algorithm. Batch-to-batch variability has prompted the development of an additional simulation layer in which an exponentially weighted moving average (EWMA) control algorithm operates between serial batch deposition sequences to adjust the operating temperature of the PECVD reactor to overcome drift in the electron density of the plasma. Application of the run-to-run (R2R) control system developed here is shown to reduce offset in the product thickness from 5% to less than 1% within 10 batches of reactor operation. Finally, we propose an extension of the EWMA algorithm to four independent, radial wafer zones in order to improve thickness uniformity in the presence of spatially non-uniform species concentrations. It is demonstrated that the produced thin films can be driven to the desired thickness set-point of 300 nm in less than 10 batches in the presence of both electron density drift and non-uniform deposition rate profiles.

© 2016 Elsevier Ltd. All rights reserved.

1. Introduction

Plasma enhanced chemical vapor deposition (PECVD) remains the dominant mechanism by which silicon based thin films are produced in both the microelectronics and solar cell industries [13]. Although moderate manufacturing costs and the possibility of extremely low operating temperatures ($\leq$525 K) allow for the widespread use of batch PECVD processing [16,31], two often neglected problems are persistent in the production of high quality amorphous silicon (*a*-Si:H) layers: the influence of reactor conditioning on the plasma chemistry [9], and the spatial non-uniformity in the thin film thickness [3] owing to gas-phase transport phenomena across the wafer. Specifically, during the initial operation of a clean PECVD reactor the plasma phase exhibits transient behavior as the interior surfaces become coated by the deposition species causing drift in the electron density profiles and in the film thickness. Second, at the reactor length scale (for example, a 20 cm wafer is used in this work) consumption and transport of deposition species across the wafer surface have been shown to cause growth rate differences greater than 19% [25,26]. Given that the efficiency of a photovoltaic absorber layer (e.g., an *a*-Si:H thin film) is strongly dependent on the film thickness [12], reduction of growth rate non-uniformities is of paramount importance. While preconditioning prior to thin film deposition (i.e., allowing the reactor surfaces to become fouled) is a well-established practice, this represents significant waste in both valuable resources and manufacturing time. In addition, the film uniformity within a single batch cannot be corrected via preconditioning alone, and has been shown to require advanced, in-situ processing techniques [6].

Recently much attention has been given to the development of model-based control schemes with the goal of improving solar cell performance through the production of textured surfaces (e.g., thin film grating) [10,11]. These models typically rely on kinetic Monte

* Corresponding author. Department of Chemical and Biomolecular Engineering, University of California, Los Angeles, CA 90095, USA.
E-mail address: pdc@seas.ucla.edu (P.D. Christofides).

http://dx.doi.org/10.1016/j.renene.2016.06.065
0960-1481/© 2016 Elsevier Ltd. All rights reserved.

Carlo (kMC) algorithms to simulate deposition processes and therefore focus on the evolution of surface microstructure in nano- to micrometer length scales. As a result, these models are unable to capture the reactor scale dynamics and cannot be applied to the problems mentioned previously which pertain to both the macroscopic and microscopic domains of batch PECVD reactor operation. Fortunately, advances in high-performance computing have made possible the modeling of multiscale processes with complex behavior and large system sizes [14,22,30]. In a pervious work of our group [6], we developed a multiscale model which provided fundamental understanding of the dynamics involved in the PECVD of *a*-Si:H thin films and allowed for quantitative prediction of product quality. In the present work, we present improvements to our original model, as well as an additional simulation domain that allows for run-to-run (R2R) control of the batch process in an effort to counteract both batch-to-batch and spatial variations in the film thickness.

More specifically, this work proposes a multiscale modeling and operation framework which is capable of not only capturing the interdependence of the gas-phase and film growth phenomena, but also allows for multi-batch operation under the implementation of a run-to-run (R2R) control algorithm. Within a single batch simulation a standard gas-phase model is used; however, the microscopic model, describing the *a*-Si:H thin film surface evolution, has been developed from the work of Tsalikis et al. [28] to be computationally efficient and account for the four dominant microscopic processes: physisorption, surface migration, hydrogen abstraction, and chemisorption. As opposed to traditional kMC formulations, surface migration has been decoupled from the other microscopic surface processes owing to its faster rate to allow for simulations on the order of thousands of monolayers without compromising fidelity to established chemical models.

At the completion of each batch simulation, a novel R2R control algorithm is applied in order to predict appropriate operating conditions for the upcoming batch. In other words, post-batch measurements of the film thickness at various radial positions are fed to an exponentially weighted moving average (EWMA) algorithm which in turn updates the temperature of the PECVD reactor within discrete zones. It is demonstrated that through appropriate tuning of the multiscale model, and application of the proposed R2R operation strategy, the thin film product can be driven to the desired thickness set-point regardless of radial position and drift within the PECVD reactor.

The structure of the manuscript is as follows: first, a detailed description of both the macroscopic gas-phase and microscopic surface models are provided. Next, extensive simulations demonstrate strong agreement between experimentally grown *a*-Si:H films and those resulting from the multiscale model proposed in this work. A total of 40 serial batch simulations conducted using the nominal process parameters (i.e., $T = 475$ K and $P = 1$ Torr) then reveal drift in the product away from the desired film thickness of 300 nm. The proposed EWMA algorithm is then applied within a single reactor zone and shown to successfully reduce film offset to within the process noise level. Finally, four concentric reactor zones are defined, each with a corresponding R2R controller and initial gas-phase concentration. In the presence of both plasma variation caused by conditioning of the reactor and spatial non-uniformity caused by consumption of the process gas, the proposed control scheme demonstrates significantly improved thickness uniformity regardless of radial position within the reactor.

2. Process description and modeling

The process under consideration in this work is a parallel plate PECVD reactor utilizing two charged electrodes designed to deposit thin films onto a single wafer placed on top of the lower electrode; see Fig. 1 (left). We employ a showerhead arrangement to distribute the influent gas stream consisting of a 9:1 mixture of hydrogen (H_2) and silane (SiH_4) throughout the chamber. Thin film growth proceeds through the production of plasma by a radio frequency (RF) power source which generates a chemically reactive mixture of radicals. These radicals (namely, SiH_3 and H) are transported to the surface via diffusion and convection where they react to form amorphous silicon (*a*-Si:H). Successful deposition requires the uniform growth of a 300 nm thick *a*-Si:H film on a wafer with a diameter of 20 cm.

Two distinct simulation regimes exist within this framework: the macroscopic gas phase which includes mass and energy balances, as well as the complex, microscopic surface interactions that dictate the structure of the silicon film of interest. Fig. 1 highlights the multiscale character of this process and the need to capture the dynamics at both scales due to the codepedency between the macroscopic and microscopic regimes. The following sections detail both the macroscopic gas-phase model and the microscopic surface model.

2.1. Gas-phase model

The twelve dominant species that lead to film growth and their corresponding thirty-four gas-phase reactions are accounted for throughout this work. A complete listing of the reactions, mechanisms and rate constants are available in Table 1. The first set of results presented in this work, within the open-loop operation section, assume that the process gas is well mixed and the rate constants do not depend on temperature. For this case a differential mass balance is used to numerically integrate the species concentrations forward with time and the resulting values are used without reference to the spatial location within the PECVD reactor. The following differential equation demonstrates the possible contributions to the mass balance for a given species:

$$\frac{dc_i}{dt} = \frac{c_i^{in}}{t_{in}} - \frac{c_i}{t_{out}} + \left[\sum_j \nu_i^j R^j\right] - \frac{1}{N_a V} r_{phys,i} + \frac{1}{N_a V} r_{abs,i}, \tag{1}$$

where c_i is the concentration in mol/cm^3 of species i, t_{in} is the inlet gas time constant defined as the reactor volume over the flow rate into the reactor, t_{out} is the outlet stream time constant defined as the reactor volume over the flow rate out of the reactor, ν_i^j is the stoichiometric coefficient for reactant i in reaction j as listed in Table 1, $r_{phys,i}$ is the rate of physisorption of species i, and $r_{abs,i}$ is the rate of abstraction of species i from the wafer surface.

The second set of results presented in this work, those referring to spatial non-uniformity in film growth, utilize a gas-phase model that includes energy and momentum balances in addition to the differential mass balance presented above. Under the assumptions of axisymmetric flow and continuum in the gas phase, mass, energy and momentum balances allow for the detailed modeling of the gas phase required in order to investigate spatial non-uniformities. The governing equations have been developed at length for CVD-type applications (e.g., [5,21,29]); however, here we apply the formulation by Armaou and Christofides [3] as radial dependence of species concentrations is needed to be accounted for due to the strong dependence of thin film thickness on photovoltaic efficiency. The mathematical model of the PECVD reactor consists of a flow velocity profile and four nonlinear dynamic diffusion-convection-reaction equations in two (radial and axial) dimensions (a set of four coupled parabolic PDEs). By treating the gas-phase as a three-dimensional stagnation flow, the evolution of the flow velocity profile within the PECVD reactor is computed from the Navier-

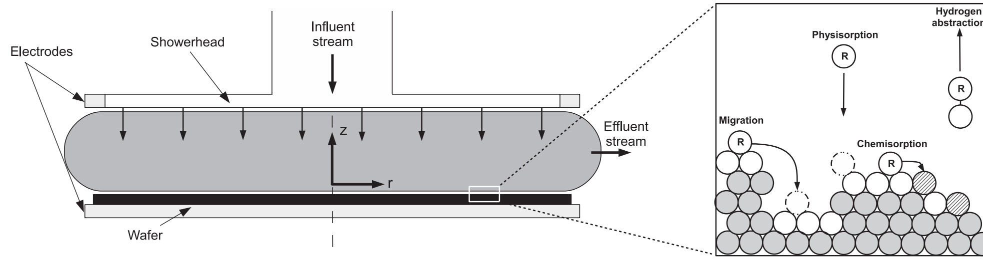

Fig. 1. Macroscopic (left) and microscopic (right) PECVD simulation regimes.

Table 1
Reactions included in the gas-phase model. Note: Rate constants have units of cm^3/sec and have been adopted from the collection prepared by Kushner et al. [17].

Reaction	Mechanism	Rate constant
R^1	$e^- + H_2 \rightarrow 2H$	7.66×10^{12}
R^2	$e^- + SiH_4 \rightarrow SiH_3 + H$	9.57×10^{13}
R^3	$e^- + SiH_4 \rightarrow SiH_3^+ + H$	3.40×10^{12}
R^4	$e^- + SiH_4 \rightarrow SiH_2 + 2H$	1.13×10^{13}
R^5	$e^- + SiH_4 \rightarrow SiH + H_2 + H$	5.62×10^{12}
R^6	$e^- + SiH_4 \rightarrow Si + H_2 + 2H$	6.70×10^{12}
R^7	$e^- + Si_2H_6 \rightarrow SiH_3 + SiH_2 + H$	2.15×10^{13}
R^8	$e^- + Si_2H_6 \rightarrow H_3SiSiH + 2H$	7.41×10^{13}
R^9	$e^- + Si_3H_8 \rightarrow H_3SiSiH + SiH_4$	3.35×10^{14}
R^{10}	$H + SiH_2 \rightarrow SiH_3$	6.68×10^{11}
R^{11}	$H + SiH_2 \rightarrow SiH + H_2$	1.20×10^{13}
R^{12}	$H + SiH_3 \rightarrow SiH_2 + H_2$	1.20×10^{13}
R^{13}	$H + SiH_4 \rightarrow SiH_3 + H_2$	1.38×10^{12}
R^{14}	$H + H_2Si = SiH_2 \rightarrow Si_2H_5$	3.01×10^{12}
R^{15}	$H + Si_2H_6 \rightarrow SiH_4 + SiH_3$	4.03×10^{12}
R^{16}	$H + Si_2H_6 \rightarrow Si_2H_5 + H_2$	7.83×10^{12}
R^{17}	$H + Si_3H_8 \rightarrow Si_2H_5 + SiH_4$	1.19×10^{12}
R^{18}	$H_2 + SiH \rightarrow SiH_3$	1.20×10^{12}
R^{19}	$H_2 + SiH_2 \rightarrow SiH_4$	1.20×10^{11}
R^{20}	$SiH_2 + SiH_4 \rightarrow Si_2H_6$	6.02×10^{12}
R^{21}	$SiH_3 + SiH_3 \rightarrow SiH_4 + SiH_2$	4.22×10^{12}
R^{22}	$SiH_3 + SiH_3 \rightarrow Si_2H_6$	6.02×10^{12}
R^{23}	$SiH + SiH_4 \rightarrow Si_2H_5$	1.51×10^{12}
R^{24}	$SiH_2 + SiH_4 \rightarrow H_3SiSiH + H_2$	6.02×10^{12}
R^{25}	$SiH_2 + Si_2H_6 \rightarrow Si_3H_8$	7.23×10^{13}
R^{26}	$SiH_2 + SiH_3 \rightarrow Si_2H_5$	2.27×10^{11}
R^{27}	$SiH_3 + SiH_3 \rightarrow SiH_4 + SiH_2$	4.06×10^{13}
R^{28}	$SiH_3 + Si_2H_6 \rightarrow SiH_4 + Si_2H_5$	1.98×10^{13}
R^{29}	$Si_2H_5 + SiH_4 \rightarrow SiH_3 + Si_2H_6$	3.01×10^{11}
R^{30}	$SiH_3 + Si_2H_5 \rightarrow Si_3H_8$	9.03×10^{13}
R^{31}	$H_3SiSiH + SiH_4 \rightarrow Si_3H_8$	6.02×10^{12}
R^{32}	$Si_2H_5 + Si_2H_5 \rightarrow Si_3H_8 + SiH_2$	9.03×10^{13}
R^{33}	$H_3SiSiH \rightarrow H_2Si = SiH_2$	2.71×10^{13}
R^{34}	$H_2Si = SiH_2 \rightarrow H_3SiSiH$	2.29×10^{10}

Stokes and continuity equations. The spatio-temporal evolution of the concentration of the species throughout the reactor is obtained by applying dynamic material balances to the gas phase and accounting for diffusive and convective mass transfer, and bulk and surface reactions. Finite-difference methods are then applied in order to discretize the spatial derivative of the species concentration in the r and z directions (z is defined as the direction normal to the wafer surface; see Fig. 1). Finally, time integration of the resulting ordinary differential equations is performed using the alternate direction implicit (ADI) method. More details on the model structure can be found in Armaou and Christofides [3], and calculated steady-state concentration profiles are discussed further in the spatial non-uniformity results section.

2.2. Surface microstructure model

The kMC methodologies applied in this work follow closely that of Crose et al. [6] and share many features common to standard kinetic Monte Carlo processes; however, simulation results generated by the multiscale model can vary widely due to discrepancies in the physical phenomena and model parameters used. As such, details of the microscopic surface interactions are presented here in full, starting with the thin film chemistry and growth kinetics.

2.2.1. Thin film growth chemistry

At the operating conditions of interest ($T = 475$ K and $P = 1$ Torr) two species dominate the interactions on the growing film, SiH_3 and H; the remaining species that exist in the gas-phase model are prohibited from depositing on the lattice surface and as a result are ignored for the remainder of the microscopic model. A schematic of the surface interactions is shown in Fig. 2, and has been verified experimentally by Perrin et al. [23] and Robertson [24]. Physisorption occurs as SiH_3 and H radicals encounter hydrogenated silicon sites ($\equiv$Si– H) at the film surface according to the following reactions:

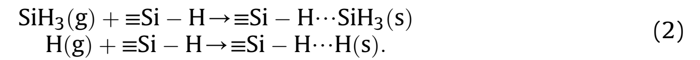

$$\begin{aligned} &SiH_3(g) + \equiv Si - H \rightarrow \equiv Si - H \cdots SiH_3(s) \\ &H(g) + \equiv Si - H \rightarrow \equiv Si - H \cdots H(s). \end{aligned} \quad (2)$$

Migration involves the rapid diffusion of physisorbed radicals across the lattice surface:

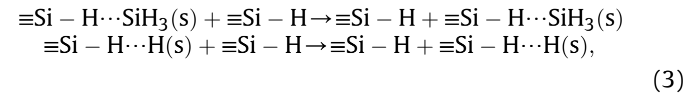

$$\begin{aligned} &\equiv Si - H \cdots SiH_3(s) + \equiv Si - H \rightarrow \equiv Si - H + \equiv Si - H \cdots SiH_3(s) \\ &\equiv Si - H \cdots H(s) + \equiv Si - H \rightarrow \equiv Si - H + \equiv Si - H \cdots H(s), \end{aligned} \quad (3)$$

eventually contributing to either hydrogen abstraction:

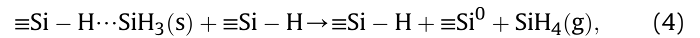

$$\equiv Si - H \cdots SiH_3(s) + \equiv Si - H \rightarrow \equiv Si - H + \equiv Si^0 + SiH_4(g), \quad (4)$$

whereby a physisorbed SiH_3 radical removes a surface hydrogen forming SiH_4 and creating a dangling bond ($\equiv Si^0$), or chemisorption at a preexisting dangling bond site according to the following reactions:

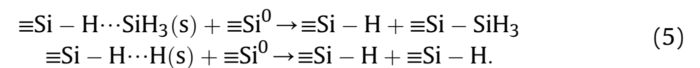

$$\begin{aligned} &\equiv Si - H \cdots SiH_3(s) + \equiv Si^0 \rightarrow \equiv Si - H + \equiv Si - SiH_3 \\ &\equiv Si - H \cdots H(s) + \equiv Si^0 \rightarrow \equiv Si - H + \equiv Si - H. \end{aligned} \quad (5)$$

Chemisorption of SiH_3 at a dangling bond site permanently grows the lattice position by one (i.e., the Si atom is fixed at that location and is no longer a candidate for migration), whereas chemisorption of H results in the surface site returning to a hydrogenated state.

2.2.2. Lattice characterization

In our recent work [6], a solid-on-solid (SOS) lattice was implemented; specifically, particles in each successive monolayer were centered above those of the previous layer and the occupation of vacant postilions was enforced in order for the height of a given lattice column to increase. Alternatively, a two-dimensional

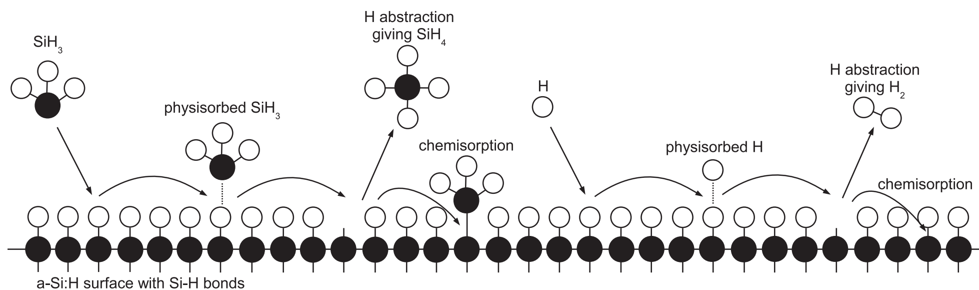

Fig. 2. Chemical model illustration showing particle-surface interactions.

triangular lattice is used in this work which allows for the deposition of SiH_3 and H particles (each deposited species is modeled by a single particle) without the restriction of SOS behavior. While an SOS square lattice does not allow for the creation of voids and porous structure within the film, a triangular lattice can produce overhangs that lead to voids while maintaining a minimum of two nearest neighbors per particle (see Fig. 3).

The size of the two-dimensional lattice is characterized by the number of lateral sites, L, and the number of monolayers, H. Using a silicon diameter of ~ 0.25 nm, the physical length of the lattice can be calculated as $0.25\times L$. Similarly, the thickness is calculated by:

$$\tau = 0.25 \cdot H \cdot \frac{\sqrt{3}}{2}, \tag{6}$$

where the factor $\sqrt{3}/2$ accounts for the reduction in thickness due to the offset monolayers (refer to Figs. 3 and 4). The number of lateral sites is chosen to be 1200 in this work as it allows for the morphology of the film to be adequately captured without being so large as to necessitate spatial variations in the gas-phase. It is important to note here that although spatial variations in the gas-phase species concentrations are introduced in later sections, they are applied at the macroscopic scale (i.e., between reactor zones) not within individual microscopic kMC simulations.

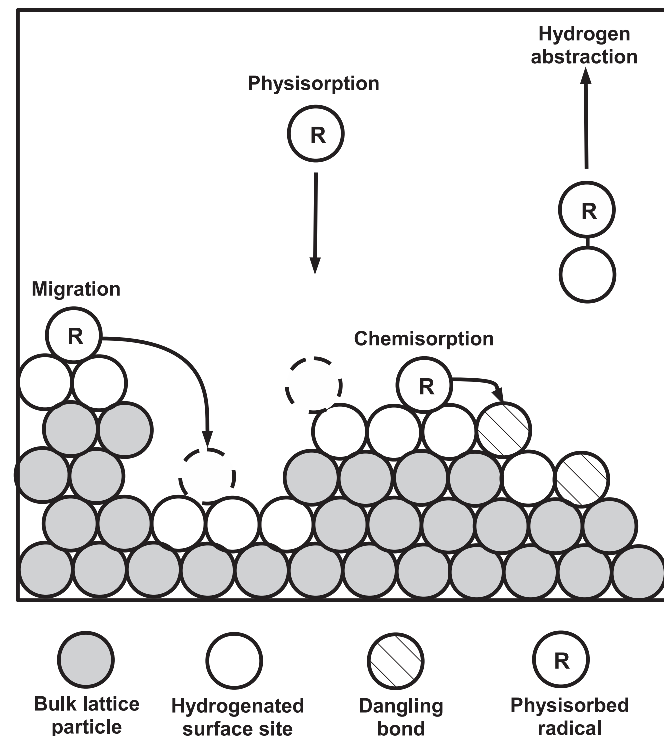

Fig. 3. Triangular lattice representation showing four microscopic processes. Processes from left to right: migration, physisorption, chemisorption, and hydrogen abstraction.

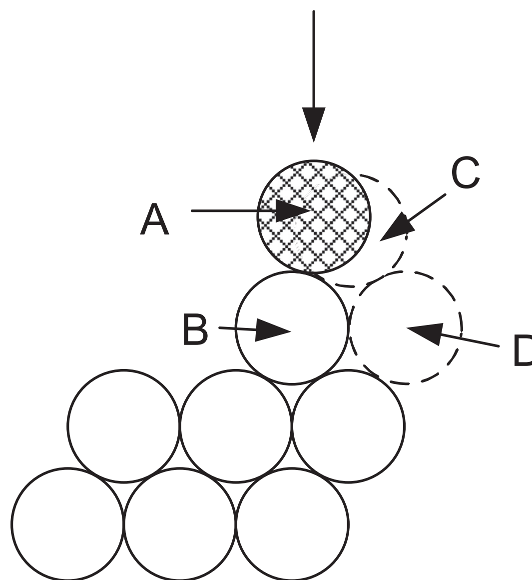

Fig. 4. Surface relaxation for physisorbed radicals. (a) Incident particle location. (b) Surface Si particle in lattice. (c) Predefined triangular lattice site with one nearest neighbor. (d) Stable position for incident particle (two nearest neighbors).

In order to enforce the restriction that all physisorbed and chemisorbed particles exist in stable, predetermined lattice locations, surface relaxation is included in the microscopic model. As shown in Fig. 4, an incident particle must first relax to a position that is centered within the defined triangular lattice. Additionally, each particle must meet the criteria of at least two nearest-neighbors to be considered stable. Unstable particles continue to relax down the lattice until a stable location is reached.

2.2.3. Relative rates formulation

A standard Arehenius-type formulation can be used to estimate the rate of thermally activated kinetic events (e.g., migration and hydrogen abstraction):

$$r_{t,i} = \nu_i e^{-E_i/k_B T}, \tag{7}$$

where ν_i is the attempt frequency prefactor (s^{-1}) and E_i is the activation energy of radical i. Frequency prefactor and activation energy values are drawn from Perrin et al. [23] to correspond to the growth of a-Si:H films via the two species deposition of SiH_3 and H.

Physisorption events follow an athermal or barrierless reaction model based on the fundamental kinetic theory of gases which

yields the following rate equation:

$$r_{a,i} = J_i s_c N_a \sigma, \quad (8)$$

where J_i is the flux of gas-phase radical i, s_c is the local sticking coefficient, N_a is the Avogadro number, and σ is the average area per surface site. J_i can be calculated via the following equations:

$$J_i = \eta_i \overline{u_i}, \quad (9)$$

$$\eta_i = \frac{p_i}{RT}, \quad (10)$$

$$\overline{u_i} = \sqrt{\frac{8k_BT}{\pi m_i}}, \quad (11)$$

where η_i is the number density of radical i (here the reactive gas-phase is assumed to be ideal), $\overline{u_i}$ is the mean radical velocity, p_i is the partial pressure of i, R is the gas constant, T is the temperature, k_B is the Boltzmann constant, and m_i is the molecular weight of radical i. Substitution of Eqs. (9)–(11) into Eqn. (8) provides the overall reaction rate for an athermal radical i:

$$r_{a,i} = \frac{p_i}{RT}\sqrt{\frac{8k_BT}{\pi m_i}} s_c N_a \sigma. \quad (12)$$

Reaction rates and sticking coefficients for the nominal process conditions (i.e., T = 475 K and P = 1 Torr) are given in Table 2. Sticking coefficients are reported for athermal reactions rather than reaction rates as these are not dependent on the gas-phase composition which varies significantly from batch to batch. The microscopic surface kinetics presented in this work have been developed from the detailed work of Tsalikis et al. [28].

2.2.4. Kinetic Monte Carlo implementation

The time evolution of the lattice microstructure is simulated using a standard n-fold kinetic Monte Carlo algorithm. The overall reaction rate is defined as

$$r_{\text{total}} = r_a^{SiH_3} + r_a^H + r_t^{abs}, \quad (13)$$

where $r_a^{SiH_3}$ is the rate of physisorption of SiH_3, r_a^H is the rate of physisorption of H, and r_t^{abs} is the rate of hydrogen abstraction forming SiH_4. Surface migration does not factor into the overall rate as it has been decoupled in the interest of computational efficiency and will be discussed at length in the next subsection. At the beginning of each kMC event a uniform random number, $\gamma_1 \in [0,1]$ is generated. If $\gamma_1 \le r_a^{SiH_3}/r_{\text{total}}$, then an SiH_3 physisorption event is executed. If $r_a^{SiH_3}/R_{\text{total}} < \gamma_1 \le (r_a^{SiH_3} + r_a^H)/r_{\text{total}}$, then a hydrogen radical is physisorbed. Finally, if $\gamma_1 > (r_a^H + r_t^{abs})/r_{\text{total}}$, then the abstraction of a surface hydrogen via SiH_3 occurs.

Both physisorption of SiH_3 and H start by selecting a random lattice site from a list of the available hydrogenated and dangling bond surface sites. If the chosen site contains a dangling bond, the radical becomes instantaneously chemisorbed causing the lattice to grow by one; otherwise, the radical is deposited on the lattice surface where it relaxes to a stable position (see Fig. 4) before becoming a candidate for migration events. Hydrogen abstraction proceeds by removing a random SiH_3 particle to form SiH_4, which is returned to the gas-phase and execution continues. Next, a second random number, γ_2, is chosen and the time step for this kMC event is calculated as

$$\delta t = \frac{-\ln(\gamma_2)}{r_{\text{total}}}, \quad (14)$$

where $\gamma_2 \in (0,1]$ is a uniform random number.

2.2.5. Decoupling surface migration

Fig. 5 highlights the disparity in the frequency of migration events relative to other event types. As a result, more than 99% of computational resources would be spent on migration alone in a traditional brute force kMC algorithm. At the standard operating conditions of T = 475 K and P = 1 Torr, it is clear that only a small fraction of simulation time contributes to events leading to film growth; consequently, the computation of rapid particle migration is decoupled from our standard n-fold kMC implementation using a two-dimensional lattice random walk process. A kMC cycle is defined by a single physisorption or abstraction event. At the completion of each cycle, a propagator is introduced to monitor the motion of physisorbed radicals. The total number of propagation steps is $N_H + N_{SiH3}$ where

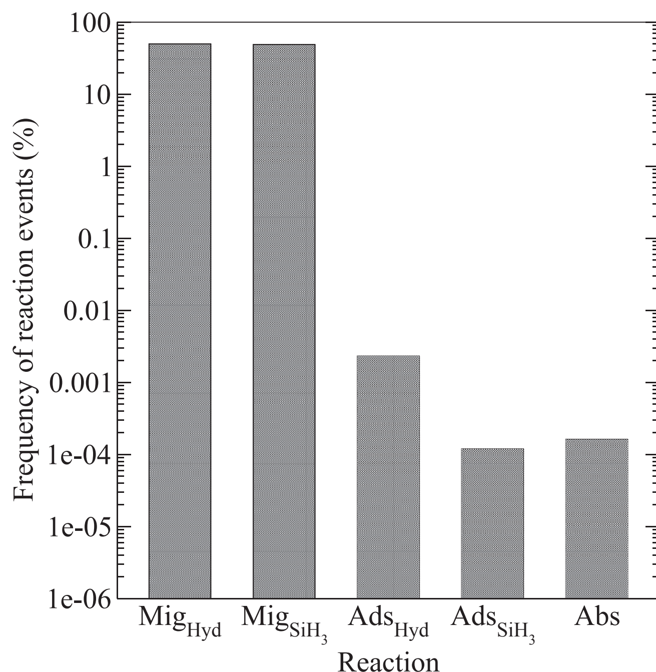

Fig. 5. Normalized frequency of reaction events within the present kMC scheme at T = 475 K, P = 1 Torr, and a SiH_4^{in} mole fraction of 0.9.

Table 2
Sticking coefficients and reaction rates composing the chemical model.

Thermally activated		Athermal reactions	
Reaction type	Reaction rate ($s^{-1}site^{-1}$)	Reaction type	Sticking coefficient
Hydrogen abstraction	3.35×10^5	SiH_3 physisorption	0.5
Hydrogen migration	1.58×10^{11}	Hydrogen physisorption	0.8
SiH_3 migration	1.16×10^{11}		

$$N_H = \frac{r_t^H}{r_a^H + r_t^{abs} + r_a^{SiH_3}}, \quad N_{SiH_3} = \frac{r_t^{SiH_3}}{r_a^H + r_t^{abs} + r_a^{SiH_3}}, \tag{15}$$

and r_t^H and $r_t^{SiH_3}$ are the thermally activated migration rates of hydrogen and silane radicals, respectively. The N_H and N_{SiH_3} propagation steps are split evenly among the n_H and n_{SiH_3} physisorbed radicals. Each radical then undergoes a two-dimensional random walk process that approximates the intricate movements of an individual particle with the bulk motion of the propagator. The procedure of the random walk process is as follows: a radical type is chosen, a random radical of the given type is selected, the weighted random walk with N_i/n_i propagation steps begins, propagation continues until either N_i/n_i steps have occurred or the radical becomes chemisorbed at a dangling bond site, the final position of the propagator is then stored as the radical's new position and this cycle continues for all $n_H + n_{SiH_3}$ physisorbed species. It is important to note that the weighting of each propagation step is such that an exponentially higher probability exists for a particle to relax down the lattice as opposed to jumping up lattice positions. In a similar manner to physisorption and hydrogen abstraction, the time increment for an individual migration step is calculated via the following equations:

$$\delta t_H = \frac{-\ln(\gamma_i)}{r_t^H}, \quad \delta t_{SiH_3} = \frac{-\ln\left(\gamma_j\right)}{r_t^{SiH_3}}. \tag{16}$$

Therefore, the total time required for all migration events, δt, is determined to be

$$\Delta t = \sum_i^{N_H} \frac{-\ln(\gamma_i)}{r_t^H} + \sum_j^{N_{SiH_3}} \frac{-\ln\left(\gamma_j\right)}{r_t^{SiH_3}}. \tag{17}$$

Film growth continues to develop under the hybrid kMC algorithm until the time allotted for a given batch has elapsed, t_{batch}.

Our methodology of decoupling the diffusive processes from the remaining kinetic events has been validated by confirming that the underlying lattice random walk process results: (1) in surface morphologies and film porosities appropriate for the chosen process parameters, and (2) growth rates on par with experimental values. Details of our model validation strategy are given in the following sections.

3. Parallel computation

Due to the size of the multiscale simulations presented in this work, the computational demands are non-trivial. Specifically, deposition of a 300 nm thick film with a horizontal dimension of 300 nm requires a simulation time on the order of days when using a single processor. The results presented in this work represent many successive batches, as well as data that has been averaged over several repeated simulations in an effort to reduce noise that occurs due to the stochastic nature of the kMC model. Consequently, computation on a single processor represents an impractical task; however, we present parallel computation here as a viable solution.

The motivations behind the use of parallel computation are threefold. As mentioned previously, the reduction in simulation time for a serial task is significant through the use of multiple processors. Second, kMC simulations inherently exhibit noise due to the stochastic nature of the model. By repeating a simulation with the same parameters numerous times we can reduce the noise and obtain more accurate, averaged values. Finally, one might want to perform many simulations at different conditions (e.g., to find suitable model parameters by testing various deposition conditions and calibrating with known experimental data).

As a brief outline, the process of creating a parallel program can be broken down into three elementary steps: (1) the original serial task is decomposed into small computational elements, (2) tasks are then distributed across multiple processors, and (3) communication between processors is orchestrated at the completion of each batch simulation. Here decomposition of the original program is achieved by separating duplicate batch simulations only, as single batch operations cannot be parallelized. The maximum achievable speedup can then be calculated as follows:

$$S(N) = \frac{1}{(1-P) + \frac{P}{N}}, \tag{18}$$

where S is the maximum speedup, P is the fraction of the program which is available for parallelization (i.e., the fraction of the serial task which involves repeated batch simulations), and N is the number of processors utilized [7].

There are two general modes used in the assignment of tasks: synchronous and asynchronous. Given the need for averaged data to be available before the next batch can be initiated, a synchronous scheme is necessary despite a slight loss in performance as compared to an asynchronous workflow in which processors are not required to wait for a batch competition before starting the next task. In other words, if it is desired to simulate n batches of PECVD reactor with ten redundant computations per batch, all ten redundant tasks must complete before the next batch in line can be initiated.

Orchestration of the assigned tasks and communication between processors is achieved using a standard message-passing interface (MPI) structure and therefore will not be discussed at this time. Further details of the parallel computation strategy employed here can be found in the recent publication of Kwon et al. [18] on which the parallel computation is based.

To demonstrate the reduction in computational time, a sample batch-to-batch simulation is run which includes 40 successive batches of PECVD of a 300 nm thick film with 10 redundant calculations per batch. The resulting computational requirements are shown in Table 3. It is clear that significant time savings are achieved as the number of cores utilized is increased. Increasing the number of cores also generates additional overhead costs due to the communication between cores and the requirement that all cores wait for the completion of the slowest redundant calculation; this is evident in the difference between the true and ideal speedup times when $n_{cores} > 1$.

4. Open-loop results

Throughout this work, simulations are conducted using a 1200 particle length ($L = 1200$) lattice with a surface that is roughened using 2400 randomly distributed deposition events to ensure that the results are not impacted by the initial configuration of the lattice. The inlet gas composition, temperature and pressure are

Table 3
Required time to complete a sample batch-to-batch simulation and the speedup time achieved.

n_{cores}	Time (hours)	Speedup (times)	Ideal speedup (times)
1	73.83	1.00	1
2	38.11	1.94	2
4	19.45	3.80	4
10	8.32	8.87	10

chosen to represent industrially used PECVD parameters and to correspond to conditions for which reliable experimental data exist. In the following two sections, simulations at the center of the PECVD reactor are used to determine the fidelity of the hybrid kMC formulation with respect to experimentally obtained film characteristics; later results will discuss operation in other reactor zones in order to highlight the importance of thickness uniformity on the efficiency of the thin film.

4.1. Plasma composition, film roughness and hydrogen content

The temporal profiles for the five species with leading concentration are shown in Fig. 6 (Note: this plot represents operation using typical process parameters, $T = 475$ K and $P = 1$ Torr). Here the inlet gas stream is maintained at 9:1 ratio of hydrogen to silane with a flow rate of 75 cm^3/s. When compared to the time scale of a complete batch ($t_{batch} \approx 285$ s), the dynamics of the species within the plasma are relatively short lived: within the first few seconds of operation all five species quickly approach their respective steady state values. Detailed plasma models have been developed by Amanatides et al. [1] and Kushner, M. [17]. which predict similar behavior for the dominant species considered here and yields confidence in the plasma composition obtained in this work.

Scanning tunneling microscopy has been used by Tanenbaum et al. [27] to accurately map the surface morphology during the growth of a 50 nm thick amorphous silicon layer deposited at 523 K and 0.54 Torr. A 1200 particle wide lattice is grown under identical conditions and the root mean square (RMS) roughness sampled at various thicknesses. The RMS roughness is calculated via the following equation:

$$R_{rms} = \sqrt{\frac{1}{L}\sum_{i=1}^{L}\left(h_i - \bar{h}\right)^2}, \tag{19}$$

where h_i is the height of the lattice at position i and $\bar{h}$ is the mean height of the lattice. As noted previously, due to the triangular arrangement of Si atoms, the height at a given position is calculated to be $\sqrt{3}/2 \cdot n$ where n is the number of layers. The results in Fig. 7 represent considerable consistency between the experimental work of Tanenbaum et al. [27] and the prediction of the multiscale model, owing further confidence to the hybrid kMC methodology used here.

Calibration of the hydrogen content within the film is accomplished by varying the deposition temperature in successive batches before postprocessing the film to determine the atomic hydrogen fraction. Comparing these values to those reported in literature [2,4,15] reveals three deposition regions with distinct behavior: (1) below 500 K the hydrogen content decreases linearly with increasing deposition temperature, (2) between 500 K and 575 K atomic hydrogen fraction remains relatively unchanged and (3) above 575 K the hydrogen capacity of the film begins to increase (see Fig. 8). While the observed range for the atomic hydrogen fraction falls within the accepted experimental region, the upturn above 575 K contradicts the expected behavior. The shift in hydrogen content at high deposition temperatures is believed to be due to competition between migration and hydrogen abstraction. When operating below 550 K, an increase in temperature will boost the migration rate for surface radicals resulting in a more dense lattice; however, at high temperatures migration down the lattice cannot overcome the rapid creation of dangling bonds leading to a porous film with increased hydrogen content. In this work the operating conditions of interest call for $T = 475$ K which lies within the linear region in which the model captures well the available experimental data.

Due to the complexity of the thin film microstructure, the hydrogen content alone cannot be used to determine the validity of the multiscale model developed here. Instead, the criteria of interest is the relationship between the porosity of the film and the hydrogen content. In this work, the site occupancy ratio (SOR) is used as a measure of porosity:

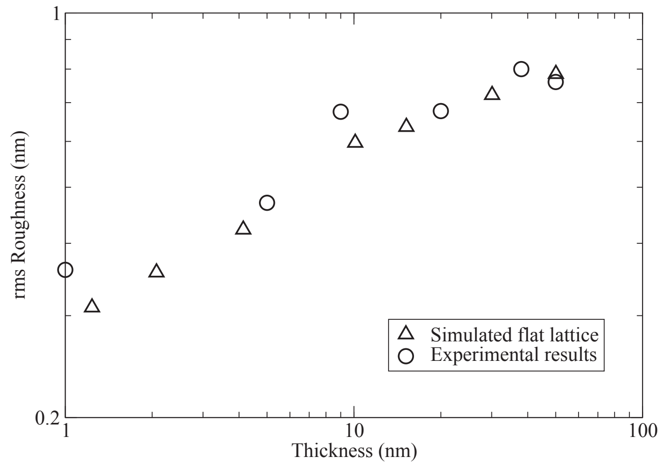

Fig. 7. Comparison of experimental and simulated rms roughness at various film thicknesses.

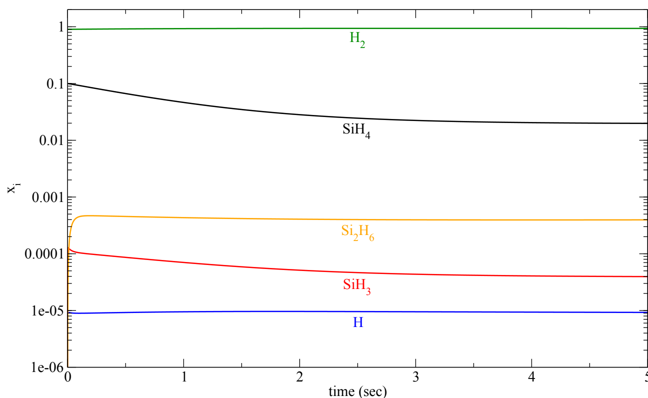

Fig. 6. Time evolution of dominant gas-phase species at $T = 475$ K and $P = 1$ Torr.

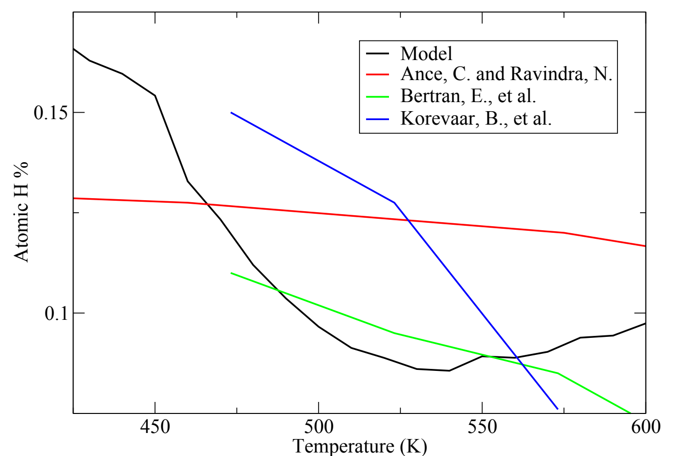

Fig. 8. Hydrogen content dependence on deposition temperature.

$$SOR = \frac{n}{LH}, \tag{20}$$

where n is the number of occupied lattice sites and LH is the total number of sites within the lattice. Given that hydrogen persists on the interior surfaces of the film it is expected that a strong correlation exists between the hydrogen content and SOR.

Fig. 9 shows the details of the film microstructure produced by the model at $T = 475$ K and $P = 1$ Torr. The scale of the lattice has been reduced here in order to demonstrate the porosity of the film, a typical simulation used in this work produces a lattice with dimensions $L = 1200$ and $H \sim 1400$ particles. The lattice shown has an SOR of 86% and an f_H of 13.8%. While Fig. 9 provides insight into the morphology of the amorphous thin film, further simulation is necessary in order to determine the accuracy of the multiscale model. Consequently, the deposition temperature is again varied and the hydrogen content of the resulting films calculated; however, in this case the hydrogen content is plotted against the SOR as experimental data is readily available for comparison. In Fig. 10 it is clear that regardless of the SOR (i.e., porosity) of a given thin film, the multiscale model developed in this work accurately reproduces the hydrogen content. In the interest of clarity, consider two simulated thin films: the first contains a distribution of small (e.g., mono- and di-) vacancies as well as less frequent, long range voids. The second simulated film may contain only a single, large pore. While the SOR of both films may be calculated to be 86%, the hydrogen content would vastly differ due to the degree of interior surface area available in each case. As such, the strong agreement in the relationship between the film SOR and hydrogen content yields confidence is the ability of the multiscale model developed in this work to reproduce the deposition of a-Si:H thin films with accurate structure and composition.

4.2. Batch-to-batch variability

Successive deposition sequences lead to fouling on the interior surfaces of the PECVD reactor causing rapid drift in the electron density of the plasma during the first several batches. The resulting drop in the concentration of SiH_3 causes the growth of the a-Si:H layer to slow yielding thin films which deviate significantly from the target thickness. This effect is demonstrated in Fig. 11 where the film thickness after 284 s of deposition is reported for 40 successive batches. By batch number 40, the reactor is considered to be fully conditioned and the electron density of the plasma is held constant

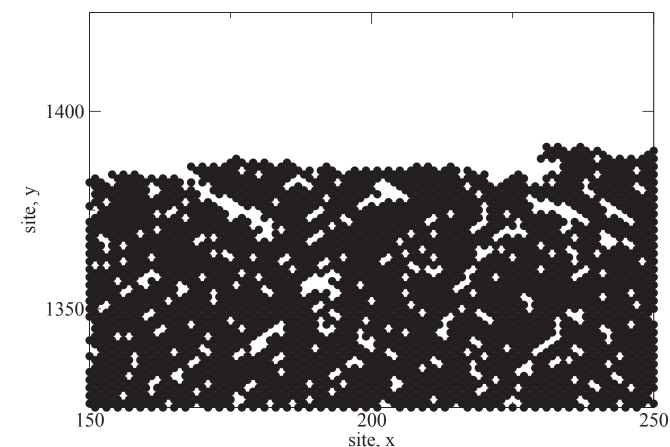

Fig. 9. Representation of voids within a typical simulated lattice. (Note: Only a fraction of the full size lattice is shown in order to highlight porosity.)

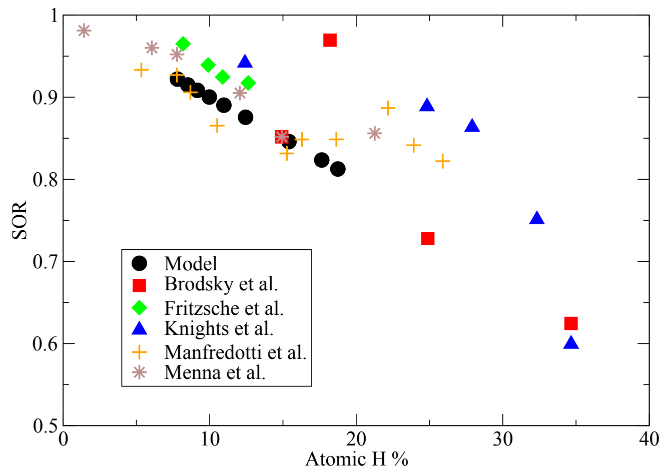

Fig. 10. Relationship between film SOR and hydrogen content.

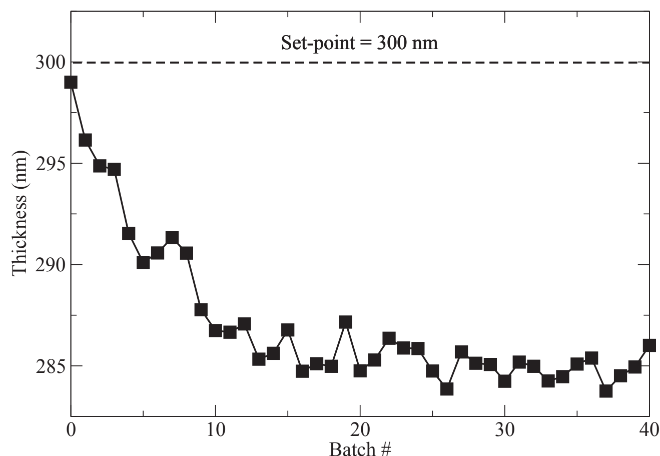

Fig. 11. Batch-to-batch drift in the film thickness.

thereafter. A deposition time of 284 s is utilized here as this represents the average time required for an a-Si:H layer to reach 300 nm thickness when simulated using the nominal process parameters discussed previously.

Films deposited in later batches show an offset of up to 5% from the target thickness of 300 nm. Due to a need for nanometer scale resolution in silicon processing industries, an offset of ~15 nm represents an unacceptable margin and has been shown to adversely affect the photovoltaic efficiency of the thin film [12]. Although the loss in efficiency due to batch-to-batch variations is relatively minor (e.g., on the order of 1%), the effect becomes greatly exaggerated when spatial variations within the PECVD reactor are accounted for. The following sections detail our efforts to reduce offset in the film thickness using a run-to-run control algorithm and spatially distributed operating temperatures.

5. R2R control of film thickness

Recently Crose et al. [6] demonstrated that the deposition rate of a-Si:H can be regulated by adjusting the temperature of the parallel plate reactor to values determined a priori by a non-linear growth rate equation. They have shown that through the use of an appropriate open-loop operation strategy, films can be deposited with uniform thickness in order to optimize photovoltaic

efficiency; however, this strategy is limited to a single batch and therefore cannot account for efficiency loss due to batch-to-batch variability in the product thickness. In this work, we build upon the concept of regulated deposition temperatures in order to develop an operation strategy which can drive the thickness of the film to the desired set-point of 300 nm in the presence of drift in the electron density of the plasma. As a result, it is first necessary to develop a relationship between the thin film growth rate and the deposition temperature within the multiscale model.

The growth rate of the film is plotted against deposition temperature in Fig. 12. The nominal process parameters call for a deposition temperature of 475 K. In the vicinity of chosen operating conditions the growth rate is shown to be proportional to the deposition temperature; consequently, a linear growth rate equation is derived using standard least squares methods:

$$G(T) = 0.0365T - 6.56\left(nm \cdot K^{-1} s^{-1}\right). \tag{21}$$

Due to the brief startup time for the reactor, the thickness (τ) of a deposited layer can be approximated as follows:

$$\tau = G(T) \cdot t_{batch}. \tag{22}$$

Together Eqns. (21) and (22) allow for the conversion between thickness measurements and temperature units required for closed-loop operation. A detailed closed-loop calculation is provided in the following section.

5.1. EWMA formulation

Given the difficulty of continuous time measurement within a PECVD reactor, a run-to-run control strategy is utilized in this work which requires only post-batch measurement [19]; [20]. Specifically, at the completion of a batch deposition process (i.e., after 284 s of simulation time) the thickness of the amorphous silicon layer is measured and fed into an EWMA (exponentially weighted moving average) algorithm which updates the temperature of the reactor for the next batch in an effort to overcome the aforementioned thickness non-uniformity. A schematic of the closed-loop operation strategy is shown in Fig. 13. Details of the EWMA algorithm (i.e., the post-batch simulation regime) are provided below:

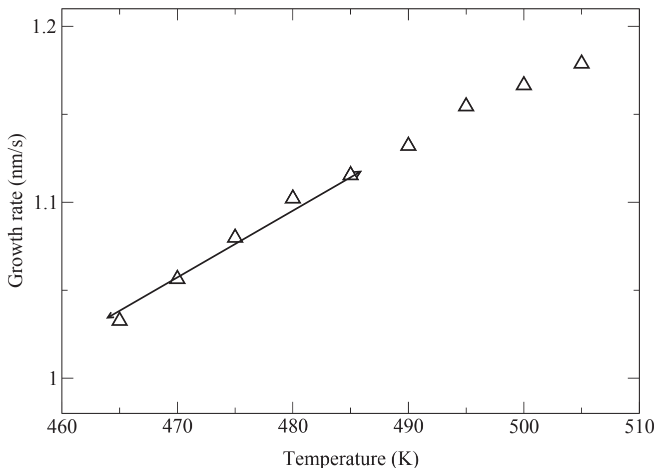

Fig. 12. Relationships between growth rate and temperature for the nominal operation parameters.

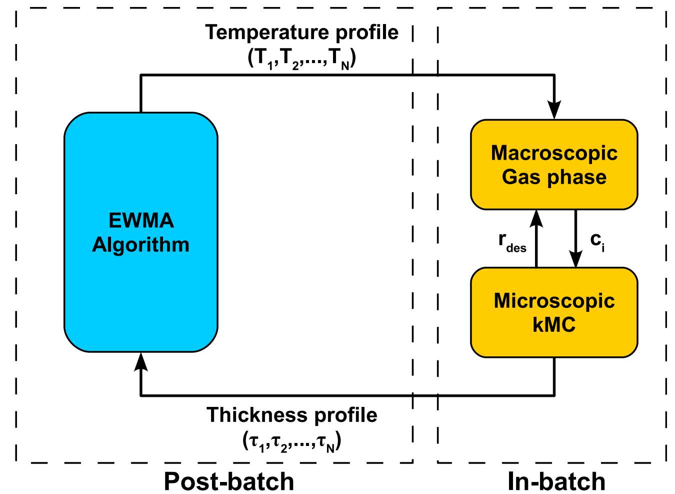

Fig. 13. Run-to-run operation of PECVD reactor.

$$\begin{aligned} \varepsilon_{k+1} &= (1-\lambda)\varepsilon_k + \lambda\left(T_{sp} - T_{model}\right) \\ T_{k+1} &= T_k + \varepsilon_{k+1}, \end{aligned} \tag{23}$$

where ε_{k+1} is the parameter correction for the $k+1$ batch, λ is the learning factor, T_{sp} is the temperature that the model predicts will be necessary to reach the set-point given t_{batch} seconds of deposition, T_{model} is the temperature that the model predicts should lead to the measured thickness, and T_{k+1} is the updated deposition temperature for the $k+1$ batch based on the previous deposition temperature and the parameter correction value, ε_{k+1}.

5.2. Closed-loop operation

Three data sets are shown in Fig. 14; the square data points represent successive batch operation without the application of the EWMA control algorithm. As stated previously, after 40 batches the product is roughly 5% below the desired set-point of 300 nm. The spherical data points represent repeated simulation using the nominal process parameters (i.e., no drift in the electron density and no control strategy applied). This provides some insight into the level of process noise and represents the threshold for perfect operation of the controller. Finally, the triangular data points represent the simulated reactor under the influence of the

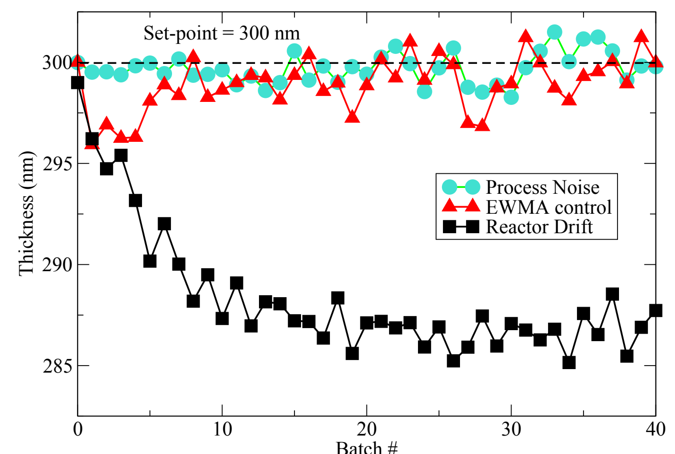

Fig. 14. Drift cancellation via a R2R controller.

proposed EWMA control algorithm. Similar to the case with no control, we see that the thickness of the product initially moves away from the set-point (batches 1–3). However, in the following batches the parameter error correction, ε, begins to counteract the effect of drift in the electron density. By batch 10 the controller has driven the product to the desired set-point and then holds the product thickness within the process noise level for all remaining batches.

As demonstrated in Fig. 15, the value of the learning factor affects the number of batches required for the thin film product to approach close to the desired set-point of 300 nm, however, in both cases (λ = 0.75 and λ = 0.25), the thickness value approaches the set-point after about 10 batches.

It is important to note here that each batch simulation treats the PECVD reactor as a single zone. In other words, the reported thickness measurements are for the entire thin film and the temperature parameters are applied equally throughout the reactor. In the following section we report an extension of the EWMA controller to multiple reactor zones in an effort to address the problem of spatial non-uniformity within a batch deposition process.

6. Spatial non-uniformity in PECVD systems

In the previous section, the discussion was focused on drift in the electron density in a batch-to-batch manufacturing process; in other words, the non-uniformity in plasma composition occurred between successive deposition sequences. Here, we address the additional problem of in-batch spatial variations (e.g., non-uniform steady-state concentration profiles in SiH_3).

As discussed in the gas-phase model, a steady-state concentration gradient for SiH_3 above the wafer surface has been calculated [3] using finite differences methods. For a 20 cm diameter wafer, a radial non-uniformity of up to 17% in the [SiH_3] is observed from the center to the edge of the silicon wafer which is expected to cause an efficiency loss of roughly 5.4% [12]; Fig. 16 demonstrates this effect for the nominal process parameters (i.e., $T = 475$ K and $P = 1$ Torr) at four distinct locations across the wafer surface.

This 5.4% level of efficiency drop corresponds to roughly the same level of thin film solar cell power output loss, as can be concluded from the dependence of voltage and current on thin film thickness reported in Ref. [12]. Carrying out a rough engineering estimate, for a typical utility-scale thin film solar cell system of 100 MW, a total installation cost of \$1.49/W – \$1.84/W is projected [8]; this cost includes not only the photovoltaic modules

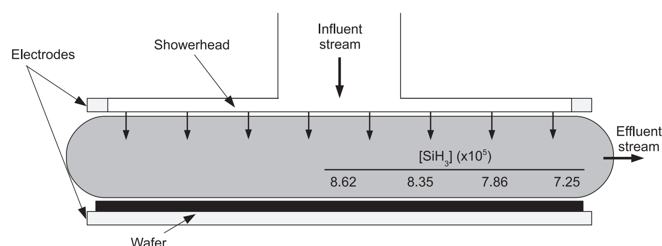

Fig. 16. Radial non-uniformity in [SiH_3] at $T = 475$ K and $P = 1$ Torr.

themselves, but also infrastructure, labor, environmental permits and other costs. Given an efficiency loss due to non-uniform deposition of thin film layers, as described above, more modules will be required in order to meet the client specification of 100 MW of power production. Assuming that the most economical features are chosen (i.e., using the lower bound for installation cost of \$1.49/W), and ignoring fixed costs, the additional photovoltaic modules (resulting from non-uniform thin film thickness) are expected to contribute on the order of \$ 8 million to the total plant cost of roughly \$ 150 million [8]. As such, significant economic benefits are available through the use of controlled operation of the PECVD reactor.

Similar to the case of batch-to-batch drift, the concentration of the deposition species of interest ([SiH_3]) is tied directly to the electron density. The resulting effect on the uniformity of the film thickness can be seen in Fig. 17 by simulating the deposition of 40 successive batches in which both batch-to-batch variation in the electron density is allowed to occur, as well as spatial non-uniformity in the steady-state concentration profiles.

The four curves in Fig. 17 represent batch-to-batch operation at four zones within the reactor without the application of an EWMA control algorithm (Note: each zone is simulated using a single lattice of length $L = 1200$). The effect of spatial non-uniformity in the concentration of SiH_3 is evident in both the initial thickness (i.e., thickness of batch 0) of each zone, as well as the total offset after 40 batches. While the product in zone 1 maintains the same 5% offset discussed earlier, zones 2–4 exhibit increased offset. After 40 batches zone 4 has drifted roughly 15% from the desired set-point of 300 nm despite the same drift in electron density being applied.

6.1. EWMA extension to concentric reactor zones

Crose et al. [6] have shown that four concentric zones can be

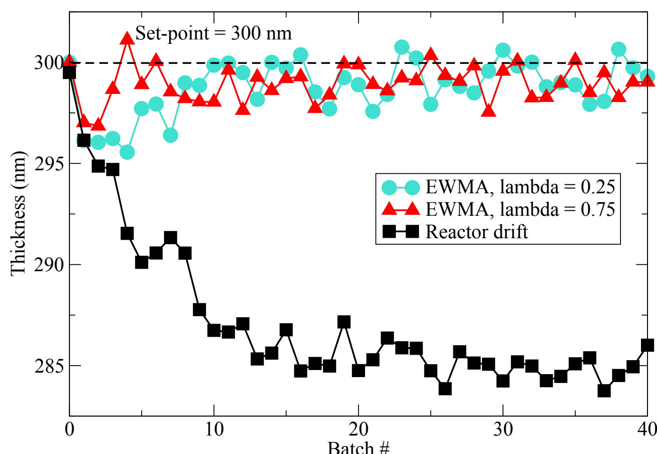

Fig. 15. Comparison of different learning factor values.

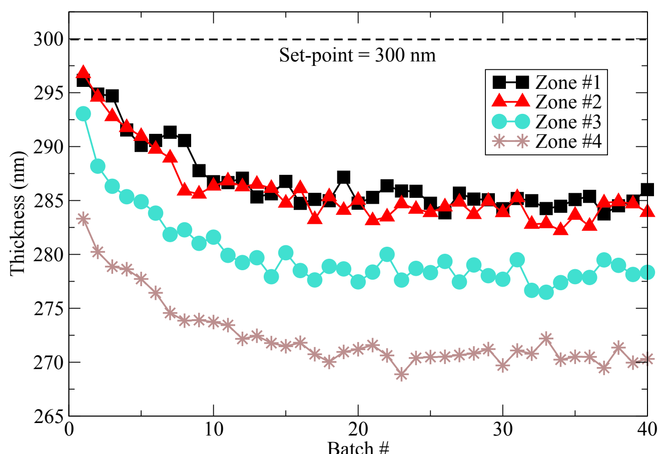

Fig. 17. Open-loop drift and spatial non-uniformity in the four radial wafer zones.

defined within the PECVD reactor as shown in Fig. 18 each with an associated heating element. Thus, the temperature in every zone can be adjusted independently in order to modulate the growth rate of the thin film. However, accurate prediction of the deposition temperature in each zone requires a corresponding growth rate relation.

Consequently, simulated films are deposited at various temperatures and the corresponding growth rates are plotted in Fig. 19. Each data set represents a different reactor zone in which the concentration of SiH_3 has been adjusted to account for the aforementioned spatial non-uniformity. The uppermost curve corresponds to the first zone and is therefore identical to the growth rate data presented in the previous section. The remaining curves demonstrate the reduction in film growth rate that occurs due to the consumption of deposition species as process gas travels radially outward toward the edge of the wafer. Linear relations are developed for each zone using standard least squares methods:

$$\begin{aligned} G(T)^1 &= 0.0365T - 6.56\left(nm\cdot K^{-1}s^{-1}\right), \\ G(T)^2 &= 0.0366T - 6.74\left(nm\cdot K^{-1}s^{-1}\right), \\ G(T)^3 &= 0.0337T - 5.54\left(nm\cdot K^{-1}s^{-1}\right), \\ G(T)^4 &= 0.0331T - 5.54\left(nm\cdot K^{-1}s^{-1}\right). \end{aligned} \tag{24}$$

$G(T)^1$ through $G(T)^4$ correspond to zones 1–4, respectively.

At this point, we can define a set of EWMA algorithms using the developed growth rate relations:

$$\begin{aligned} \varepsilon_{k+1}^i &= (1-\lambda)\varepsilon_k^i + \lambda\left(T_{sp}^i - T_{model}^i\right) \\ T_{k+1}^i &= T_k^i + \varepsilon_{k+1}^i. \end{aligned} \tag{25}$$

Recall, through the assumption of time invariant growth rates we can write the thickness as $\tau^i = G(T)^i \cdot t_{batch}$ to allow for conversion between post-batch measurements and temperature values necessary for the controlled input.

In the interest of clarity, Fig. 20(a) is provided which details the paths of the controlled inputs, T^i. In each zone, the deposition temperature increases from batch to batch to overcome the reduction in electron density that occurs as the reactor becomes conditioned. As expected, a significantly higher temperature must be applied in the outermost zones in order to accommodate for the reduced growth rate due to consumption of SiH_3. The four matching curves in Fig. 20(b) show the performance of the extended EWMA control algorithm. By batch number 10, the thin film thickness in each reactor zone is driven to the desired set-point and then maintained within the process noise level for all successive batches.

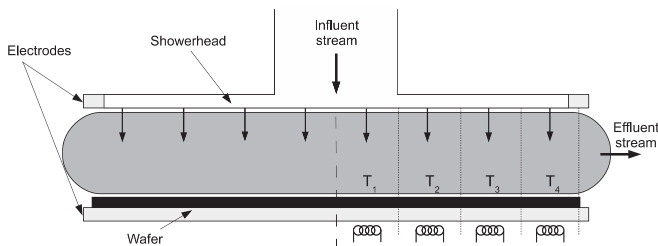

Fig. 18. Discrete PECVD reactor schematic showing four independent, concentric substrate temperature control zones.

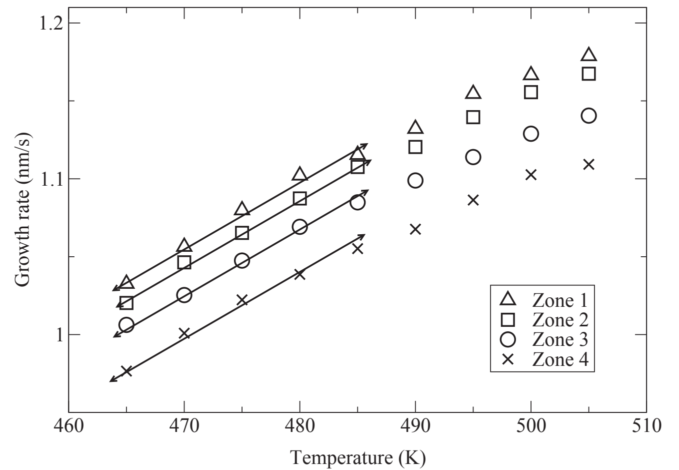

Fig. 19. Relationships between growth rate and temperature for each reactor zone.

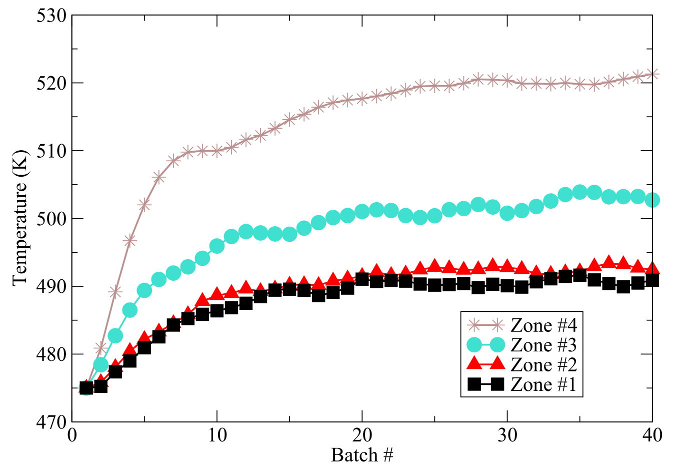

(a) Control action computed by EWMA algorithm.

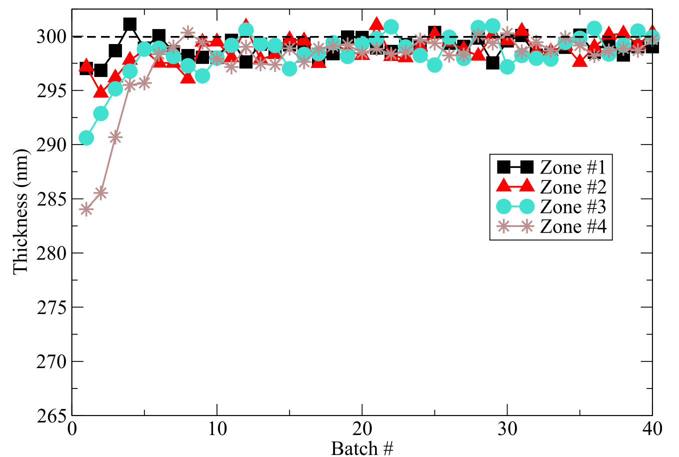

(b) Closed-loop operation via EWMA control algorithm.

Fig. 20. R2R control of four independent wafer zones.

7. Conclusions

In this work, a multiscale modeling and run-to-run framework for the PECVD of thin film solar cells with uniform thickness and

reduced batch-to-batch variability was proposed. The macroscopic gas-phase utilizes mass, momentum and energy balances, under the assumption of continuum to provide the plasma composition necessary in the calculation of deposition rate profiles. Additionally, the proposed microscopic model is based on a novel hybrid kinetic Monte Carlo algorithm that has been shown to be both computationally efficient and to reproduce thin film morphologies on par with experimental observations. Together the macroscopic and microscopic simulation have yielded insights and data that have been used to develop a closed-loop operation strategy which has been shown to improve film quality and to reduce batch-to-batch variability caused by drift during the conditioning phase of reactor operation. Specifically, an EWMA (exponentially weighted moving average) algorithm has been introduced which calculates substrate temperatures that mitigate the effect of batch-to-batch reactor variability. Simulations of open-loop operation suggest an offset of 5% from the desired set-point of 300 nm film thickness due to reactor variability. The proposed EWMA control strategy was applied first to a PECVD reactor with a single heating control element which allowed for the temperature to be adjusted post-batch to counteract drift in the electron density, thereby reducing the product offset to $< 1\%$. Lastly, an extension of the proposed EWMA control algorithm was demonstrated which allows for in batch variation in the deposition temperature within concentric reactor zones in an effort to reduce spatial non-uniformity in the thin film thickness. Simulations demonstrate both a reduction in the product offset to less than 1% as well as radially uniform films within 10 batches of closed-loop operation.

Acknowledgements

Financial support from the National Science Foundation (NSF), CBET-1262812, is gratefully acknowledged.

References

[1] E. Amanatides, S. Stamou, D. Mataras, Gas phase and surface kinetics in plasma enhanced chemical vapor deposition of microscrystalline silicon: the combined effect of RF power and hydrogen dilution, J. Appl. Phys. 90 (2001) 5786–5797.
[2] C. Ance, N. Ravindra, Departure of hydrogen from a-Si:H, Phys. Status Solidi 77 (1983) 241–248.
[3] A. Armaou, P.D. Christofides, Plasma enhanced chemical vapor deposition: modeling and control, Chem. Eng. Sci. 54 (1999) 3305–3314.
[4] E. Bertran, J. Andujar, A. Canillas, C. Roch, J. Serra, G. Sardin, Effects of deposition temperature on properties of r.f. glow discharge amorphous silicon thin films, Thin Solid Films 205 (1991) 140–145.
[5] P.D. Christofides, A. Armaou, Control and optimization of multiscale process systems, Comput. Chem. Eng. 30 (2006) 1670–1686.
[6] M. Crose, J.S.I. Kwon, M. Nayhouse, D. Ni, P.D. Christofides, Multiscale modeling and operation of PECVD of thin film solar cells, Chem. Eng. Sci. 136 (2015) 50–61.
[7] D. Culler, J. Singh, A. Gupta, Parallel Computer Architecture: a Hardware/software Approach, Gulf Professional Publishing, 1999.
[8] R. Fu, T. James, D. Chung, D. Gagne, A. Lopez, A. Dobos, Economic competitiveness of US utility-scale photovoltaics systems in 2015: regional cost modeling of installed cost ($(/W)$/kWh), in: Photovoltaic Specialist Conference (PVSC), 2015 IEEE 42nd, IEEE, 2015, pp. 1–11.
[9] O. Gabriel, S. Kirner, M. Klick, B. Stannowski, R. Schlatmann, Plasma monitoring and PECVD process control in thin film silicon-based solar cell manufacturing, EPJ Photovolt. 55202 (2014) 1–9.
[10] J. Huang, G. Orkoulas, P.D. Christofides, Modeling and control of Transparent Conducting Oxide layer surface morphology for improved light trapping, Chem. Eng. Sci. 74 (2012a) 135–147.
[11] J. Huang, G. Orkoulas, P.D. Christofides, Surface morphology control of transparent conducting oxide layers for improved light trapping using wafer grating and feedback control, Chem. Eng. Sci. 81 (2012b) 191–201.
[12] M. Kabir, S. Shahahmadi, V. Lim, S. Zaidi, K. Sopian, N. Amin, Amorphous silicon single-junction thin-film solar cell exceeding 10% efficiency by design optimization, Int. J. Photoenergy 2012 (2012) 1–7.
[13] W. Kern, Thin Film Processes II, Academic Press, 1991.
[14] I.G. Kevrekidis, C.W. Gear, G. Hummer, Equation-free: the computer-aided analysis of complex multiscale systems, AIChE J. 50 (2004) 1346–1355.
[15] B. Korevaar, G. Adriaenssens, A. Smets, W. Kessels, H.Z. Song, M. van de Sanden, D. Schram, High hole drif mobility in a-Si:H deposited at high growth rates for solar cell application, J. Non Cryst. Solids 266–269 (2000) 380–384.
[16] M. Kreiger, D. Shonnard, J. Pearce, Life cycle analysis of silane recycling in amorphous silicon-based solar photovoltaic manufacturing, Resour. Conserv. Recycl. 70 (2013) 44–49.
[17] M. Kushner, A model for the discharge kinetics and plasma chemistry during plasma enhanced chemical vapor deposition of amorphous silicon, J. Appl. Phys. 63 (1988) 2532–2551.
[18] J.S.I. Kwon, M. Nayhouse, P.D. Christofides, Multiscale, multidomain modeling and parallel computation: application to crystal shape evolution in crystallization, Ind. Eng. Chem. Res. 54 (2015a) 11903–11914.
[19] J.S.I. Kwon, M. Nayhouse, G. Orkoulas, D. Ni, P.D. Christofides, A method for handling batch-to-batch parametric drift using moving horizon estimation: application to run-to-run mpc of batch crystallization, Chem. Eng. Sci. 127 (2015b) 210–219.
[20] J.S.I. Kwon, M. Nayhouse, G. Orkoulas, D. Ni, P.D. Christofides, Run-to-run-based model predictive control of protein crystal shape in batch crystallization, Ind. Eng. Chem. Res. 54 (2015c) 4293–4302.
[21] R. Lam, D.G. Vlachos, Multiscale model for epitaxial growth of films: growth mode transition, Phys. Rev. B 64 (2001) 035401.
[22] D. Maroudas, Multiscale modeling of hard materials: challenges and opportunities for chemical engineering, AIChE J. 46 (2000) 878–882.
[23] J. Perrin, M. Shiratani, P. Kae-Nune, H. Videlot, J. Jolly, J. Guillon, Surface reaction probabilities and kinetics of H, SiH_3, Si_2H_5, CH_3, and C_2H_5 during deposition of α-Si:H and α-C: H from H_2, SiH_4, and CH_4 discharges, J. Vac. Sci. Technol. A 16 (1998) 278–289.
[24] J. Robertson, Deposition mechanism of hydrogenated amorphous silicon, J. Appl. Phys. 87 (2000) 2608–2617.
[25] L. Sansonnens, J. Bondkowski, S. Mousel, J. Schmitt, V. Cassagne, Development of a numerical simulation tool to study uniformity of large area PECVD film processing, Thin Solid Films 427 (2003) 21–26.
[26] U. Stephan, J. Kuske, H. Gruger, A. Kottwitz, Problems of power feeding in large area PECVD of amorphous silicon, Mat. Res. Soc. Symp. Proc. 557 (1999) 157–162.
[27] D. Tanenbaum, A. Laracuente, A. Gallagher, Surface roughening during plasma-enhanced chemical-vapor deposition of hydrogenated amorphous silicon on crystal silicon substrates, Phys. Rev. B 56 (1997) 4243–4250.
[28] D. Tsalikis, C. Baig, V. Mavrantzas, E. Amanatides, D. Mataras, A hybrid kinetic Monte Carlo method for simulating silicon films grown by plasma-enhanced chemical vapor deposition, J. Chem. Phys. 139 (2013) 204706.
[29] D.G. Vlachos, Multiscale integration hybrid algorithms for homogeneous-heterogeneous reactors, AIChE J. 43 (1997) 3031–3041.
[30] D.G. Vlachos, A review of multiscale analysis: examples from systems biology, materials engineering, and other fluid-surface interacting systems, Adv. Chem. Eng. 30 (2005) 1–61.
[31] C. Yang, L. Smith, C. Arthur, G. Parsons, Stability of low-temperature amorphous silicon thin film transistors formed on glass and transparent plastic substrates, J. Vac. Sci. Technol. B 18 (2000) 683–689.